Finite element evaluations of the mechanical properties of polycaprolactone/hydroxyapatite scaffolds by direct ink writing: Effects of pore geometry

Bin Zhang[a,1], Liwei Guo[a,1], Hongyi Chen[a] , Yiannis Ventikos[a],

Roger J. Narayan [b,*], Jie Huang[a,**]

[a] Department of Mechanical Engineering, University College London, London, UK

[b] Joint Department of Biomedical Engineering, University of North Carolina and North Carolina State University, Raleigh, NC, USA

[*]Corresponding author. E-mail address: roger_narayan@unc.edu

[**]Corresponding author. E-mail address: jie.huang@ucl.ac.uk

[1]*The first two authors contributed equally to this work.*

1

Abstract

Osteochondral (OC) defects usually involve the damage of both the cartilage and its underneath subchondral bone. In recent years, tissue engineering (TE) has become the most promising method that combines scaffolds, growth factors, and cells for the repair of OC defects. An ideal OC scaffold should have a gradient structure to match the hierarchical mechanical properties of natural OC tissue. To satisfy such requirements, 3D printing, e.g., direct ink writing (DIW), has emerged as a technology for precise and customized scaffold fabrication with optimized structures and mechanical properties. In this study, finite element simulations were applied to investigate the effects of pore geometry on the mechanical properties of 3D printed scaffolds. Scaffold specimens with different lay-down angles, filament diameters, inter-filament spacing, and layer overlaps were simulated in compressive loading conditions. The results showed that Young's moduli of scaffolds decreased linearly with increasing scaffold porosity. The orthotropic characteristics increased as the lay-down angle decreased from 90° to 15°. Moreover, gradient transitions within a wide range of strain magnitudes were achieved in a single construct by assembling layers with different lay-down angles. The results provide quantitative relationships between pore geometry and mechanical properties of lattice scaffolds, and demonstrate that the hierarchical mechanical properties of natural OC tissue can be mimicked by tuning the porosity and local lay-down angles in 3D printed scaffolds.

1 Introduction

Osteochondral (OC) interfaces are specialized and integrated structures in the joints between bones in the human body; these interfaces consist of multiple tissue elements, mainly including cartilage, calcified cartilage, and bone. OC injuries can lead to joint malfunction and ultimately to the development of degenerative diseases such as osteoarthritis (Mobasheri *et al.*, 2014, Rodrigues *et al.*, 2011). OC defects have poor regenerative potential; clinical findings indicate that there is no existing medication to substantially promote the healing process; surgical procedures (e.g., autografts) are normally required for OC tissue repairing (Schroeder and Mosheiff, 2011, Chiang and Jiang, 2009). However, these interventions are limited by the supply of autograft tissue in the human body (Jakob *et al.*, 2002).

To date, tissue engineering approaches have been used to create three-dimensional (3D) porous scaffolds out of biocompatible materials; these porous scaffolds facilitate adhesion, proliferation, differentiation, and migration of cells to facilitate tissue regeneration (Shuai *et al.*, 2020b, Feng *et al.*, 2019). Due to the physiological interfacial transition from cartilage to subchondral bone in natural OC tissue, the most important consideration is that the scaffold features (e.g., pore size and pore shape) should (a) mimic the gradient characteristics to aid nutrient delivery and tissue regeneration, and (b) possess compatible mechanical properties with the host tissue to achieve optimal structural integrity (Athanasiou *et al.*, 1994, Boschetti *et al.*, 2004, Shuai *et al.*, 2020c). Natural OC tissue is composed of the cortical bone, the cancellous bone, and the cartilage, which generally become more ductile towards the cartilage region with changed orientation of collagen fibers (Gibson, 1985, Sabree *et al.*, 2015, Athanasiou

et al., 1994, Boschetti *et al*., 2004, Sophia Fox *et al*., 2009). This complicated structure poses a challenge for scaffold design, especially in terms of mimicking the transition of mechanical properties between different regions (Shuai *et al*., 2020a).

One method to develop OC tissue scaffolds involves using biphasic, triphasic or multiphasic layers, or gradient structures to mimic the bone and cartilaginous phases of natural OC tissue (Schek *et al*., 2004). Schaefer *et al*. (2000) described scaffolds made of polyglycolic acid (PGA), poly-lactic-co-glycolic acid (PLGA) and polyethylene glycol (PEG), respectively. Those two constructs were sutured together. Jiang *et al*. (2010) presented a triphasic scaffold, where (a) the bone phase was based on PLGA and bioactive glass composite, (b) the cartilage phase was created using agarose hydrogel, and (c) the intermediate phase contained a combination of agarose hydrogel (similar to the cartilage phase), PLGA, and bioactive glass. The three phases were fabricated separately and then pre-integrated as a scaffold using a customized mold.

Previous reseach indicated that biphasic or triphasic scaffolds yielded good repairs of OC defects *in vitro* or *in vivo*; however, in most cases, the fabrication of those scaffolds requires joining individual phases together using suturing, glue, or press fitting, which could result in delamination after transplantation due to insufficient bond strength (Nooeaid *et al*., 2012, Raghunath *et al*., 2007). To overcome the problem of delamination and obtain functional gradient in a single construct, Dormer *et al*. (2010) developed new fabrication methods to produce gradient PLGA scaffolds controlled by a designed program. The *in vitro* experiments showed increased cell attachment, production of extracellular matrix, glycosaminoglycan, and collagen content, as well as alkaline phosphatase activity of mesenchymal stem cells in gradient scaffolds with pore

size increased from 70 to 220 µm in comparison with those having a uniform pore size. However, traditional fabrication methods (e.g., salt leaching, gas forming, and freeze-drying) have limited control of pore geometries, mechanical properties, and interconnectivity. Such limitations may lead to a non-uniform distribution of cells, which can prevent the cells from properly functioning (Do *et al*., 2015, Wüst *et al*., 2011).

3D printing (3DP) has emerged as a new technology in the field of tissue engineering due to its capability to create (a) personalized scaffolds for patients and (b) scaffolds with well-defined porous features (Yang *et al*., 2018). Among many 3D printing methods, direct ink writing (DIW) has been widely used to fabricate tissue scaffolds since this processing approach can be performed at ambient temperature, enabling the incorporation of biomolecule and/or cells (Trachtenberg *et al*., 2017, Park *et al*., 2011, Gonçalves *et al*., 2016). Using DIW, the scaffolds can be fabricated according to the design that is specified in computer-aided design (CAD) models (Athanasiou *et al*., 1994, Boschetti *et al*., 2004). Moreover, the scaffold porosity as well as interconnectivity for nutrient delivery and tissue regeneration can be readily modified (Reichert *et al*., 2011, Hutmacher and Cool, 2007). An example of using DIW to fabricate a polycaprolactone (PCL)/hydroxyapatite (HA) scaffold based on a CAD model is shown in Figure 1. The PCL/HA ink was formulated by adding nanoHA particles into a PCL solution; the nanoHA particles were prepared in advance by a wet-precipitation method (Huang *et al*., 2010). The DIW processing approach allows for accurate control of the ink extrusion rate and motion of the nozzle by a computer program. The final DIW-printed scaffold is shown in Figure 1c.
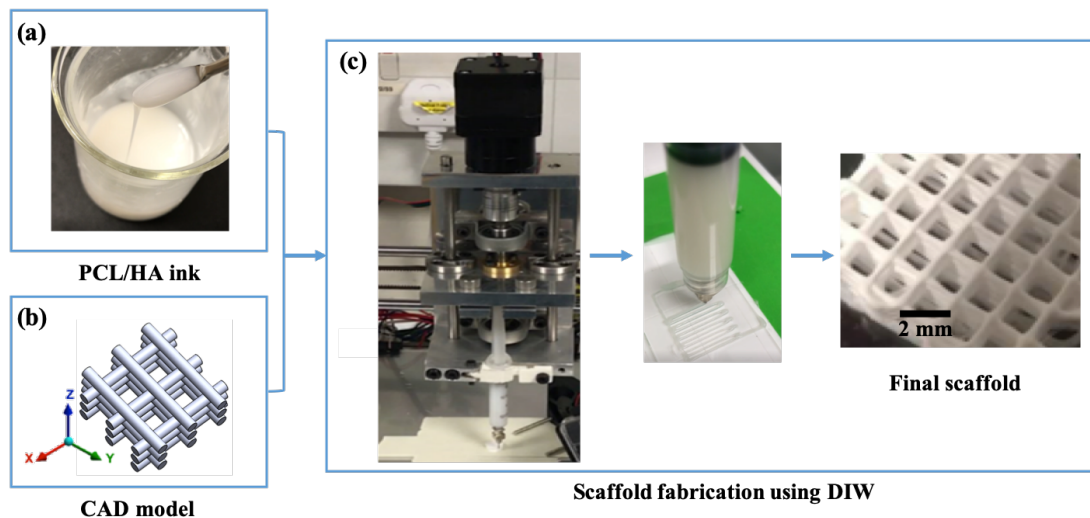
Figure 1: Schematic of printing a PCL/HA scaffold using the DIW technique.

Computational modeling has shown great potential in biomedical engineering research (Chen *et al*., 2018, Guo *et al*., 2017, Guo *et al*., 2020), including the development of bone scaffolds (Lacroix and Prendergast, 2002, Kaul *et al*., 2015). It offers a precise and easily adjustable approach for comparing the mechanical properties of different scaffold designs in a timely and economical manner. Byrne *et al*. (2007) applied fully 3D computational modeling approach to simulate tissue differentiation and bone regeneration in scaffolds as a function of porosity, Young's modulus, and dissolution rate. Cahill *et al*. (2009) used finite element analyses to compare the mechanical properties between 3D printed and CAD designed scaffolds to identify the key factors that affect the mechanical properties of scaffold structures. San Cheong *et al*. (2018) proposed new finite element algorithms to predict bone ingrowth and model the effect of surface modification on osteoconduction in porous scaffolds. Entezari *et al*. (2019) developed a simple and efficient computational modeling approach for characterizing strain and total strain energy in bond scaffolds.

The finite element method (FEM) is one of the most commonly used numerical methods to simulate the mechanical properties of 3D scaffolds. Sandino et al. (2008) analyzed the strain distribution within calcium phosphate scaffolds and biodegradable glass scaffolds. Melchels et al. (2010) designed CAD models with various structures and evaluated the mechanical properties by simulation of compressive testing. Ali and Sen (2017) analyzed the effective elastic modulus, compressive strength, permeability, and fluid flow-induced wall shear stress as a function of porosity. Hendrikson et al. (2017) showed the significant impact of scaffold architecture on mechanical strain distribution. Naghieh et al. (2018) developed both linear and non-linear FE models to predict the elastic modulus of alginate scaffolds. Rodríguez-Montaño et al. (2018) used poroelastic models to investigate the influence of scaffold design parameters on the mechanical response in different load regimes. Wang et al. (2018) evaluated the mechanical properties of porous Ti scaffolds with different pore structures.

Most previous studies focused on the influence of pore size and porosity on the mechanical properties of scaffolds (Naghieh et al., 2016, Eshraghi and Das, 2010, Diego et al., 2007, Lacroix et al., 2006). To the best of the authors' knowledge, the effect of pore shape has not been systemically investigated. Hence, the effects of various pore shapes on the mechanical properties of scaffolds are investigated with the aims to achieve a gradient of mechanical properties in a single scaffold construct while still maintaining an interconnected pore network. In this paper, the finite element method is used to evaluate the effects of pore parameters (e.g., porosity and pore shape) on mechanical properties of the scaffolds prior to scaffold fabrication with customized DIW. In addition to the global mechanical properties (e.g., Young's modulus), this

study also seeks to understand the local strain distributions in various scaffold structures.

2 Materials and methods

2.1 Design of the scaffold structure

Two types of scaffolds were designed: the first type is a cubic layered lattice structure with a single lay-down angle. The second type is a complex structure by assembling sections of different lay-down angles.

2.1.1 Single lay-down angle

The woodpile scaffold was designed as a cubic layered structure, based on the design criteria in the literature (Hulbert *et al*., 1970, S. Van Bael 2012). The design criteria are also consistent with the DIW fabrication process, in which the scaffold is printed in a layer-by-layer manner. Each layer of the scaffold is of a square shape and has a lattice structure (Figure 2); therefore, the entire 3D lattice scaffold forms a porous structure. The edge length of the cubic scaffold is 9 mm ($D_1 = D_2 = L = 9$ mm).

The geometric properties of the lattice scaffold are defined as follows. The scaffold pore size in the *XY* plane is the inter-filament spacing d_{xy}, i.e., the distance between two adjacent filaments on the same layer, where the filament diameter is d. The scaffold pore size d_z in the direction perpendicular to the *XY* plane is the distance between two layers of filaments with the same orientation. The layer overlap f refers to the overlapping distance between two adjacent layers. For each layer, the filaments are placed in a parallel arrangement (i.e., they are all arranged in one direction); the filament orientations between adjacent layers are different in order to form a lattice

structure. The angle formed by the two filament orientations between adjacent layers is defined as the lay-down angle (viewed from the *XY* plane); it is measured with respect to the *X* direction. Six different lay-down angles, ranging from 15° to 90° (Figure 2), are investigated in this paper. More specifically, the effects of pore geometry are investigated from two aspects: (a) the porosity, which can be modified by changing the filament diameter d, inter-filament spacing d_{xy} within the same layer, and the layer overlap f between layers, as well as (b) the pore shape, which can be modified by varying the lay-down angle from 15° to 90°.
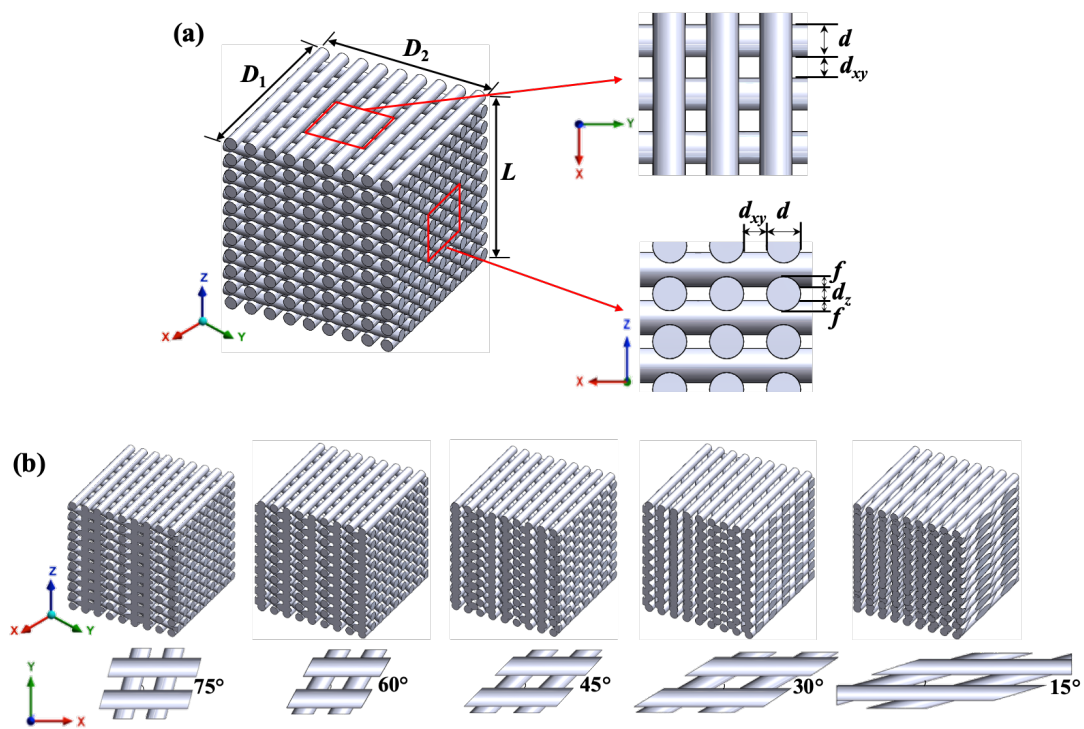

Figure 2: (a) A 3D woodpile scaffold with a lay-down angel of 90° and local views to demonstrate the design parameters; (b) Various lay-down angles and associated unit cells in the *XY* plane.

2.1.2 Multiple lay-down angles

Natural osteochondral (OC) tissue covering the joint surface has a transition from hard bone tissue to soft cartilage; this structure exhibits hierarchical/gradient mechanical characteristics (Dorcemus and Nukavarapu, 2014). A tissue scaffold for the treatment

of OC lesion needs to pierce into the hard bone and be in contact with both cartilage and bone; as such, it should mimic the gradient mechanical properties from cartilage to a transition zone of calcified cartilage and further to bone (Vacanti and Langer, 1999, Reichert *et al*., 2011, Hutmacher and Cool, 2007). Therefore, it is better to achieve the required mechanical properties of the natural OC tissue in a single scaffold construct; benefits of this approach include easier implantation and lower cost in terms of design and fabrication. For this objective, a complex scaffold structure was created by assembling six sections of layered lattices; each section has a single lay-down angle of 15°, 30°, 45°, 60°, 75°, and 90°, respectively (Figure 3). All of the sections have the same number of layers (i.e., equal height in the longitudinal Z direction). The overall height of the model is 15.34 mm. The cross-section (XY plane) of the scaffold is a square (9 mm × 9 mm) and remain the same in the Z direction. Other design parameters, including the filament diameter (600 μm), inter-filament spacing (400 μm) and layer overlap (180 μm), remain constant throughout the entire scaffold.
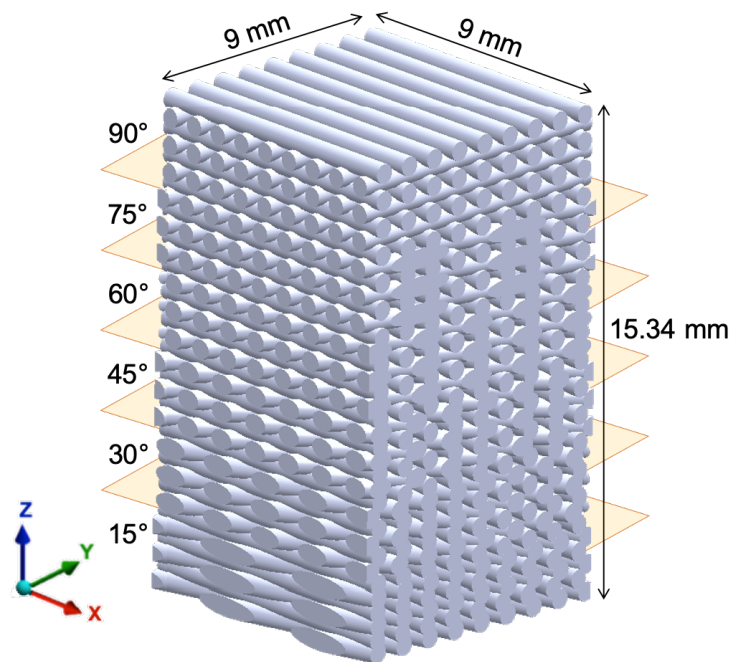

Figure 3: A complex scaffold structure assembled by six sections of different lay-down angles in a single construct; each section has three layers.

2.2 Finite element model

Finite element simulations were conducted to investigate the effects of pore geometry on Young's modulus (i.e., the apparent elastic modulus of the scaffold), compressive strength, and strain distributions in the lattice scaffolds. All of the models used in finite element modeling are discretized by linear tetrahedral elements. The numerical compression tests are implemented by displacement-controlled boundary conditions. The setup of a compression test in the vertical direction is shown in Figure 4. The scaffold specimen is placed between two rigid plates. The bottom plate is fixed; a displacement-controlled boundary condition is applied at the top plate to represent the compressive loading condition. A bonded contact model is applied between the specimen and the loading plates (i.e., no sliding or separation is allowed). The displacement rate is 1 mm/min, which is a typical quasi-static loading rate for bone and biomaterial testing (Luczynski *et al*., 2013, Brynk *et al*., 2011, Feng *et al*., 2018, Shuai *et al*., 2020a). The final displacement is set as an equivalent vertical strain of 0.5% in the specimen, which is within the range of elastic deformation for this composite material.

In terms of material properties, the loading plates are assumed to be rigid; as such, the material properties are irrelevant. The material for scaffolds is poly (ε-caprolactone) (PCL)/nanohydroxyapatite (HA) composite. For simplicity, a bilinear isotropic hardening model is used in the simulations. The Young's modulus value of the PCL/HA bulk material (40 MPa) and the yield strength (3 MPa) were obtained from mechanical compression testing of cylindrical specimens. It is worth mentioning that other researchers (Luczynski *et al*., 2013, Luczynski *et al*., 2012) obtained different values of Young's modulus for similar scaffolds that were made out of other bulk materials

(e.g., poly-l-lactide (PLLA)/tri-calcium phosphate (TCP) composite); however, the absolute value of material Young's modulus does not affect the correlation between the mechanical properties of scaffolds and structural differences (as shown in the Supplementary Figure). The Poisson's ratio is set as 0.3 (Eshraghi and Das, 2010, Van Rietbergen et al., 1999). The PCL/HA bulk material is assumed to be homogeneous. Some previous researchers used heterogeneous material properties (Luczynski et al., 2012, Scheiner et al., 2009, Szlazak et al., 2019) and found that the homogeneity assumption may lead to overestimation of the elastic modulus values in FE modeling of biomaterials (Renders et al., 2008, Blanchard et al., 2013, Dejaco et al., 2012). However, a more detailed comparison (Blanchard et al., 2013) using a micromechanics model (Königsberger et al., 2020) concluded that the difference in mechanical properties between homogeneous and heterogeneous models becomes smaller if the scaffold has a periodic structure and is subjected to uniform loading conditions. Since the scaffolds investigated in this paper satisfy such requirements, the homogeneity assumption was adopted. All the simulations were conducted using ANSYS Workbench 17.0 (ANSYS, Inc., Canonsburg, USA).
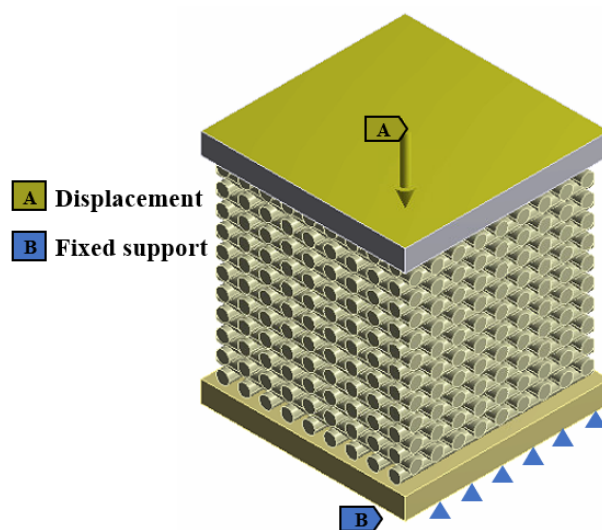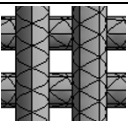

Figure 4: Setup for the finite element simulations. An example of compressive loading in the vertical direction is shown. The bottom plate is fixed, and the top plate moves downwards in the vertical direction.

3 Results and discussion

3.1 Mesh sensitivity test

The effect of the mesh size on the finite element modeling results was firstly investigated on the scaffold specimens with a lay-down angle of 90° under compressive loading (Figure 4). A series of different size meshes are generated based on the same geometry; all of the other parameters are identical. The Young's modulus of the scaffold is calculated as an output variable to measure the convergence when the mesh size is decreased. The values of Young's modulus and computational time of different meshes are listed in Table 1. The results show that the Young's modulus changes by 12% if the minimum element size is reduced from 0.4 to 0.125 mm; it only changes by 0.7% if the mesh size is further reduced to 0.1 mm. However, using a mesh size of 0.1 mm requires 1.5 times more computational time than using a mesh size of 0.125 mm. Therefore, it is suggested that imposing a minimum edge size of 0.125 mm for the tetrahedral elements generates finite element solutions with good accuracy and affordable computational time; this mesh size is used in all of the simulations.

Table 1: Young's modulus and computational time of five different meshes.

	Mesh 1	Mesh 2	Mesh3	Mesh 4	Mesh 5
Mesh of the 90° lattice scaffold					
Minimum element size (mm)	0.4	0.2	0.15	0.125	0.1
Number of tetrahedral elements	100 701	409 429	889 496	1 379 586	3 047 672
CPU time (min)	25	30	50	80	120
Young's modulus (MPa)	16.2	15.25	14.78	14.2	14.1

3.2 Effects of porosity on Young's modulus

Porosity is an important factor that affects the mechanical properties of scaffolds (Loh and Choong, 2013); it is calculated as the percentage of the void space to the total volume occupied by the outer boundary of the porous scaffold. There are three key parameters that control the porosity of a 3D layered lattice scaffold: the filament diameter d, the inter-filament spacing d_{xy} within the same layer, and the layer overlap f between layers (Figure 2). In this section, different combinations of various values for these three parameters are evaluated to create a range of porosities for understanding the effects of various porosities on the Young's moduli of scaffolds. All of the scaffold specimens simulated in this section have a lay-down angle of 90°.

First, different porosities are achieved by changing the design parameters within the *XY* plane (parallel to the layers). Nine scaffold specimens with different combinations of filament diameters and inter-filament spacing were created. Three values are chosen for the filament diameter – 600 μm, 400 μm and 300 μm; for each filament diameter, three values of inter-filament spacing are assigned – 400 μm, 700 μm and 1000 μm (Figure 5a). Next the filament diameter is fixed at 600 μm, and the inter-filament spacing is fixed at 400 μm; different porosities are obtained by changing the design parameter in the *Z* direction (perpendicular to the layers). Seven scaffolds were created by varying the layer overlap from 60 to 300 μm (Figure 5b). It can be seen from Figure 5a that the Young's modulus decreases when the filament diameter decreases and the inter-filament spacing increases. This effect can be attributed to the column-like behavior of filament junctions when undergoing compressive deformation (Domingos et al., 2013). In other words, for a specific area in the *XY* plane (parallel to the layers), the scaffold with a larger filament diameter or smaller inter-filament spacing has more

load-bearing capacity, hence increasing the stiffness of the scaffold. Figure 5b shows

that the Young's modulus increases as the layer overlap increases. The overlapping

regions between layers provide the main path for load transfer in the Z direction

perpendicular to the layers; therefore, larger overlap means that the layers are more

closely bonded, thus making the scaffold structure stiffer.
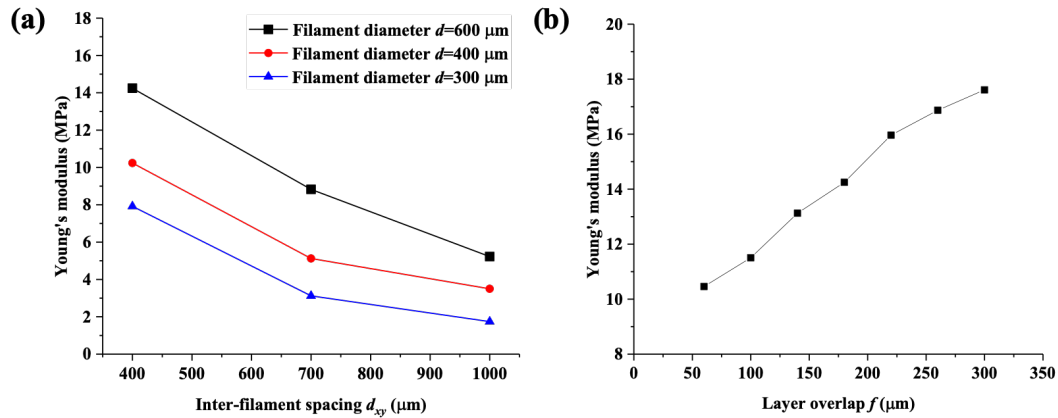
Figure 5. Plots of Young's modulus versus the filament diameter and the inter-filament spacing (a), and Young's modulus versus the layer overlap (b).

The porosity values are calculated for the sixteen specimens; the relationship between

porosity and Young's modulus is shown in Figure 6. The result shows that Young's

modulus decreases linearly with increasing scaffold porosity; these results are

consistent with previous findings for bone (Hellmich *et al.*, 2004) and bone replacement

biomaterials (Fritsch *et al.*, 2009, Kariem *et al.*, 2015, Fritsch *et al.*, 2010). As porosity

increases, there are more voids in the lattice structure, making the scaffold less bonded

and easier to deform (i.e., lower Young's modulus). Figure 6 also shows that the range

of Young's modulus values obtained from finite element modeling covers the range of

Young's modulus values of natural osteochondral tissue; a porosity value of

approximately 60% separates the scaffold application between that of cancellous bone

repair and that of cartilage repair. By manipulating the parameters used to design the

15

scaffolds, the desired Young's modulus of the scaffold can be customized to match specific osteochondral tissue.

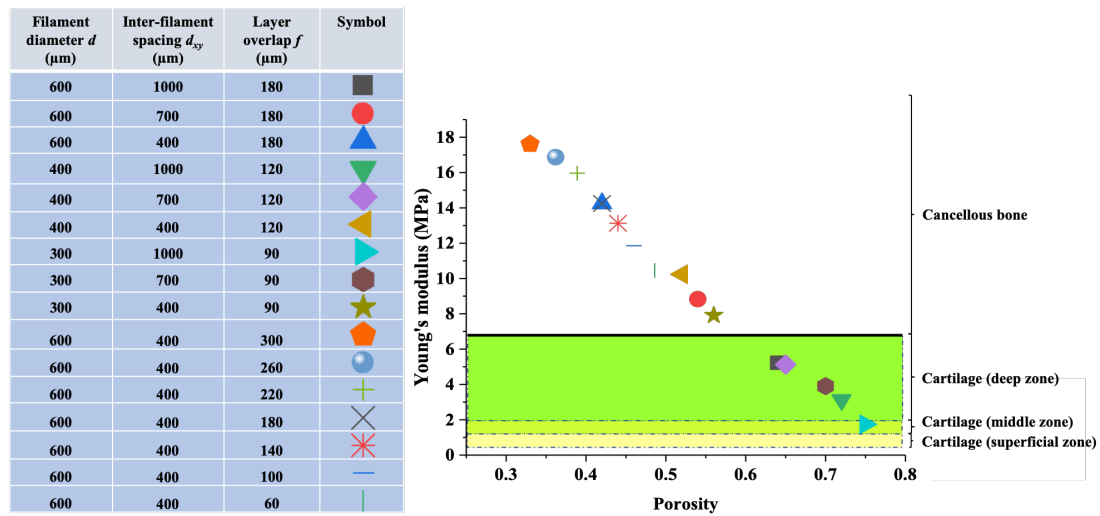| Filament diameter d (µm)	Inter-filament spacing d_{xy} (µm)	Layer overlap f (µm)	Symbol
600	1000	180	■
600	700	180	●
600	400	180	▲
400	1000	120	▼
400	700	120	◆
400	400	120	◀
300	1000	90	▶
300	700	90	⬢
300	400	90	★
600	400	300	⬠
600	400	260	⬤
600	400	220	+
600	400	180	✕
600	400	140	✳
600	400	100	—
600	400	60		

Figure 6: Plot of Young's modulus versus porosity.

3.3 Effects of pore shape

The pore shape is characterized by the lay-down angle in the layered scaffold. The focus here is to analyze the correlation between the lay-down angle and the anisotropic property of scaffolds from two perspectives. First, six cubic scaffold specimens were created with a single lay-down angle of 15°, 30°, 45°, 60°, 75°, and 90°, respectively; each layer of all scaffolds has the same number of filaments. The only difference between these scaffolds is the lay-down angle; all of the other parameters, including the filament diameter (600 µm), inter-filament spacing (400 µm) and layer overlap (180 µm), remain constant. All the specimens have a similar porosity (42%). The anisotropic property is analyzed by the difference in Young's moduli when the cubic scaffolds are compressed in three orthogonal directions, respectively, by finite element modeling. Second, a complex layered lattice scaffold was created by assembling six sections with different lay-down angles (15°, 30°, 45°, 60°, 75°, and 90°) in a single construct. The anisotropic property is analyzed by the difference in the local strain distributions when the scaffold is simulated under compression loading conditions.

16

3.3.1 Single lay-down angle

Six cubic scaffold specimens with a single lay-down angle of 15°, 30°, 45°, 60°, 75°, and 90° were compressed in X, Y and Z directions, respectively, using displacement-controlled boundary conditions. Here the Z direction is named as the longitudinal direction because it is perpendicular to the filament layers; the other two directions (X and Y) in the Cartesian coordinate system are named the transverse directions, which are parallel to the filament layers. The lay-down angle is defined with respect to the X direction.

The mechanical properties of scaffolds are normally characterized by stiffness (Young's modulus) and compressive strength (Shuai *et al*., 2017, Shuai *et al*., 2018, Feng *et al*., 2014, Rezwan *et al*., 2006, Chen *et al*., 2011), which are presented in Figure 7. In the longitudinal Z direction, the Young's modulus slightly decreases at lower lay-down angles. Filaments with a smaller lay-down angle have more asymmetric alignment of the connecting joints in the Z direction, which affects their force resistance. Hence, under compression in the Z direction, filaments with smaller lay-down angles can more easily slide from each other, thus increasing the deformability of the scaffold. It is also worth pointing out that the Young's modulus value of the 90° scaffold in the longitudinal Z direction is slightly smaller than the values in the two transverse directions (X and Y directions). This result can be explained by the different load transfer mechanisms when the 90° scaffold is compressed in different directions. When compressed in the longitudinal Z direction, the compressive loading is supported by the overlapping regions between layers; when compressed in either the X or Y direction, the loading is mainly supported by the filaments themselves, which are stiffer and behave like columns, therefore generating smaller deformation.

17

Different lay-down angles mainly affect the pore shape in the XY plane; as such, the anisotropic characteristic is most prominent in the XY plane. When the specimen is compressed in the X direction, the Young's modulus increases when the lay-down angle is reduced from 90° to 15°. More specifically, the Young's modulus is 21.47 MPa at 15°, which is 34% greater than that of the 90° scaffold. When the lay-down angle is small (e.g., 15°), the filaments of all the layers are laid in one dominant direction, which forms a bundle of filaments and behaves like a column structure to sustain the compressive loading. On the other hand, when the specimen is compressed in the Y direction, Young's modulus decreases as the lay-down angle is reduced. The lower Young's modulus values at smaller lay-down angles can be attributed to the large deformation of a spring-like structure. When the filaments are arranged almost parallel to the ones in adjacent layers, the load transfer in the direction perpendicular to the filaments follows a spiral path, which can generate large deformation under compressive loading and lead to a relatively low Young's modulus. Moreover, it is worth noting that the Young's moduli of 30° and 15° scaffolds compressed in the Y direction are less than 1 MPa; these values are in the range of the Young's modulus value for cartilage tissue.

The anisotropic nature of the lattice scaffolds in the transverse plane is reflected by the difference in Young's moduli in X and Y directions, so the scaffolds can be classified as orthotropic structures (Sutcu, 1992). The orthotropic effect increases when the lay-down angle decreases from 90° to 15°, indicating that the lattice scaffold can adapt to different requirements of anisotropy simply by rotating the orientation of filaments. In general, the trabecular network is complicated; for example, a highly oriented and columnar architecture is observed in the vertebrae and tibia. This kind of trabecular

bone is highly anisotropic, and Young's modulus values can be different in the longitudinal and transverse directions (Williams and Lewis, 1982). In contrast, the cancellous bone can be essentially isotropic in regions such as the proximal part of the bovine humerus (Kaplan *et al*., 1985). In general, the isotropic nature of scaffold facilitates its use in bone defects regardless of its orientation (Gómez *et al*., 2013, Gómez *et al*., 2016). The scaffold with a lay-down angle of 90° is more suitable for such an environment where isotropic mechanical properties are necessary. On the other hand, if the bone tissue is anisotropic, then the design of the scaffold can be adjusted by tuning the lay-down angle based on the extent of anisotropy.

The compressive strength is recorded as the stress when the scaffold structure reaches yielding on the stress-strain curve. The compressive strength of cubic scaffolds decreases with the lay-down angle varying from 90° to 15° when loaded in the longitudinal Z direction or in the transverse Y direction; the compressive strength shows a plateau around 45° when compressed in the transverse X direction. As a layered structure, the scaffold is more stable if the filaments are arranged in orthogonal directions within the layer when compressed in the Z direction (perpendicular to the layers). When compressed in the transverse directions (X or Y), the filaments that are aligned with the compressive direction provide the most support to sustain the loading. Therefore, the compressive strength in the Y direction decreases when the lay-down angle (defined with respect to the X direction) changes from 90° to 15° as the orientation of filaments rotates from the Y direction to the X direction. When compressed in the X direction, however, the structure lacks constraints in the lateral direction to maintain compressive stability when all the filaments are aligned dominantly in the X direction

(e.g., 15°); as such, the compressive strength drops after reaching a plateau between 60° and 45°.
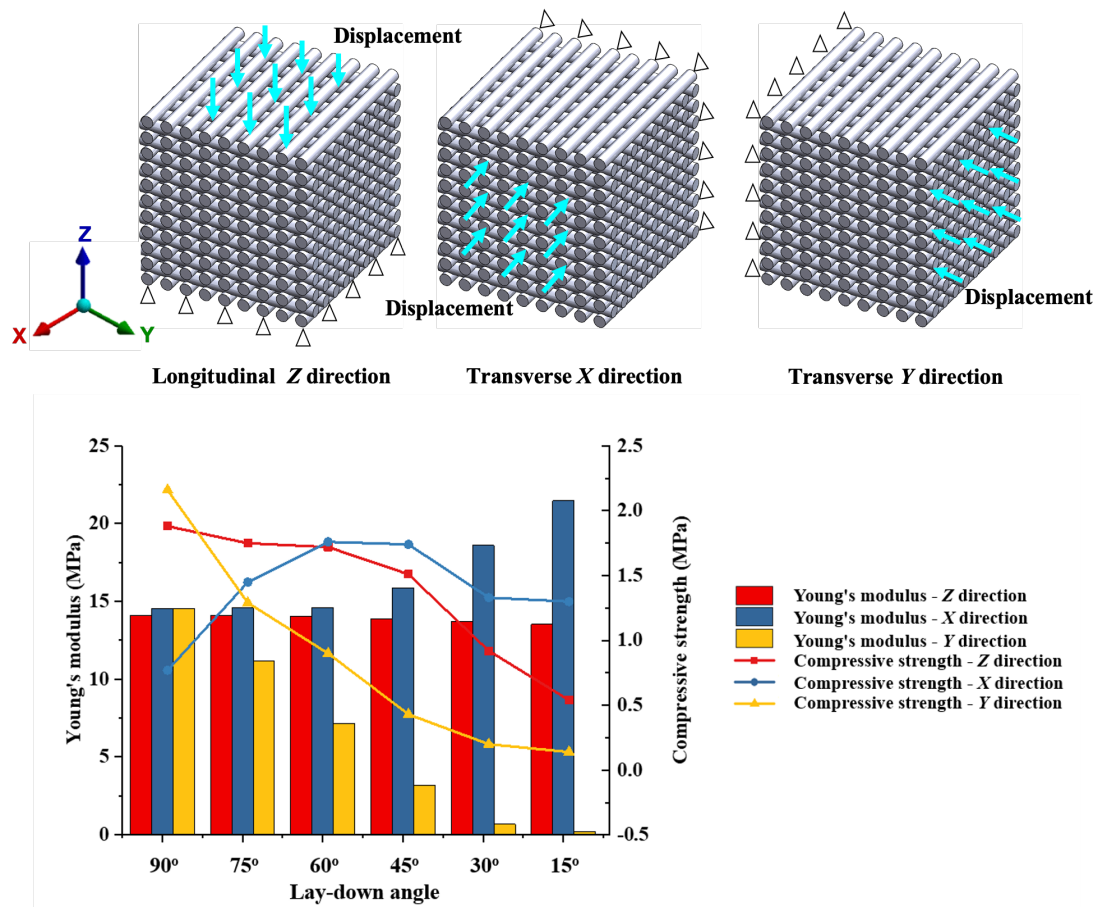
Figure 7: Young's moduli and compressive strength values of cubic scaffolds with different lay-down angles compressed in three orthogonal directions, respectively. The lay-down angle is defined with respect to the *X* direction.

3.3.2 Multiple lay-down angles

In this section, a complex layered scaffold was created by assembling individual sections of six different lay-down angles – 15°, 30°, 45°, 60°, 75°, and 90°. As the anisotropy mainly exists in the transverse *XY* plane, it is compressed in the transverse *X* and *Y* directions, respectively.

In the previous section, the anisotropic nature of the scaffold is mainly reflected in the difference in Young's moduli between different compressive loading directions. The assembled complex scaffold presented here retains this characteristic because the local stiffness of each section still depends on the loading direction applied to that individual section; the bonding regions between sections of different lay-down angles behave as transition zones. In this section, the anisotropic property is analyzed from another perspective: strain distribution. The strain distribution is also an important factor because the strains generated from mechanical loading are transmitted to cells attached on the surfaces of scaffolds, which in turn stimulate various types of cell differentiation according to the deformation magnitude (Meyer *et al*., 2006). Different strain magnitudes may lead to chondrogenic or osteogenic differentiation to rebuild the functions of damaged OC tissue (Carter *et al*., 1998, Prendergast *et al*., 1997). The assembled scaffold is placed in a uniform loading environment (i.e., no variation of loading between different sections), and the strain distributions from different sections of the scaffold are examined.

Figure shows the maximum principal strain on the surface of the central layer in each of the six sections from 90° to 15°. The light grey filaments in the background represent the underlying layer, where the filaments are arranged in a fixed orientation (i.e., along the X direction) (Figure 3). The grey "holes" within the filaments are the overlapping areas (joints) with adjacent layers in the longitudinal Z direction. Since the strain contours are only visualized on the filament surfaces, these overlapping areas lie within the filaments; as such, the strains are not shown. It can be seen from Figure that the strain magnitudes are generally higher around these joints, which is consistent with previous findings of localized stress and strain peaks at the joints (Luczynski *et al*.,

2012, Szlazak *et al*., 2019). Although the pore shape becomes increasingly skewed as the lay-down angle decreases from 90° to 15°, all of the scaffold specimens exhibit periodic strain distributions due to the uniform and repetitive pattern of cell arrangement in the lattice structure. The section with higher strains supports more load than the other lay-down angles. For example, when the specimen is compressed in the *X* direction, it is the 15° section that has the highest strain magnitude because the filament orientation is the closest to the compressive direction (Figure f); when compressed in the *Y* direction, the 90° section sustains most of the load and therefore has the largest strain (Figure g). As the 45° orientation exhibits the same angle on *X* and *Y* directions, the 45° section shows similar patterns of strain distributions when compressed in either *X* or *Y* direction (Figure 8d and j).

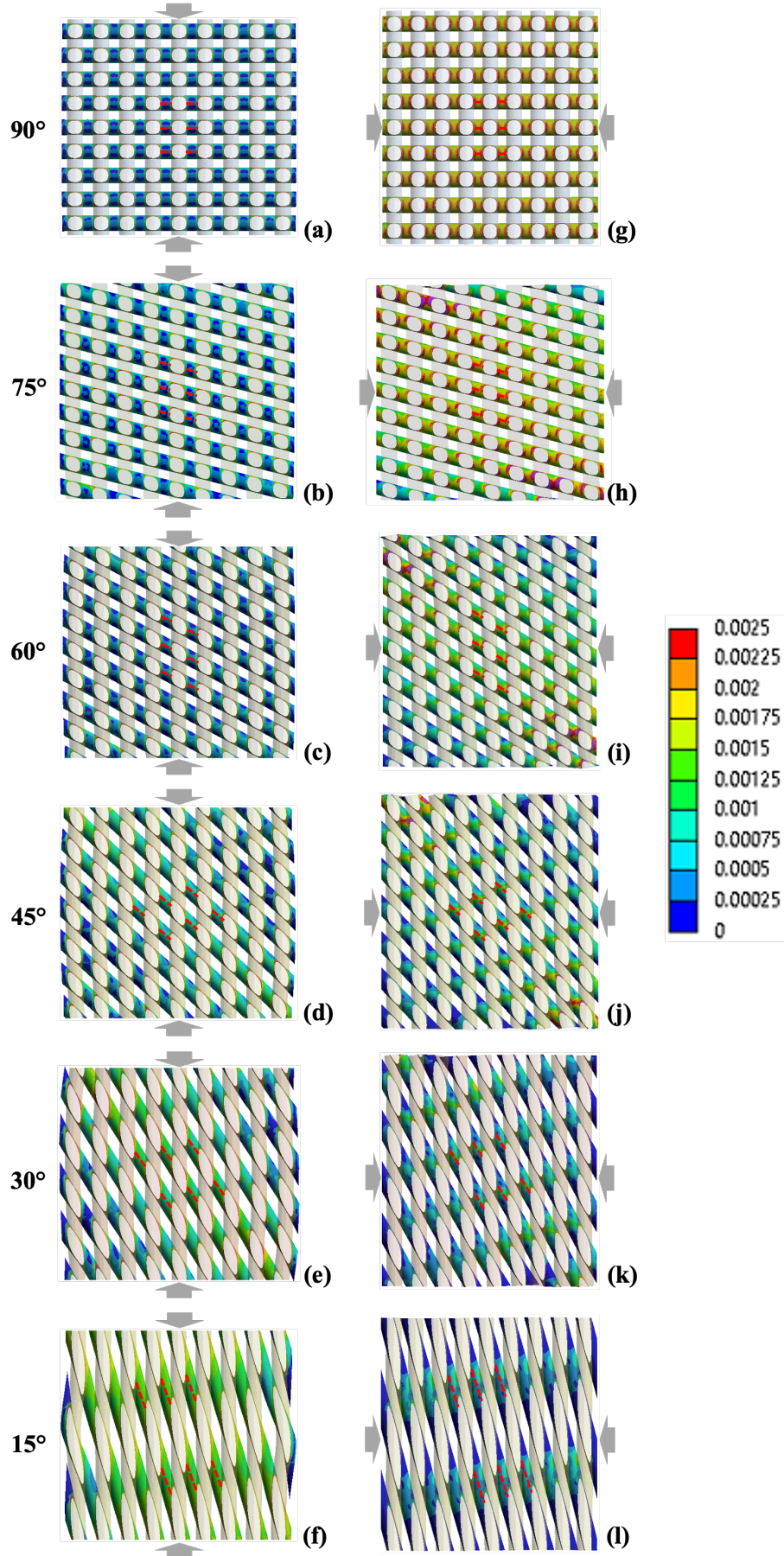**Compression in the *X* direction   Compression in the *Y* direction**

Figure 8: Maximum principal strain on the filament surface of the central layer in each section (three layers) of the assembled scaffold specimen. The lay-down angle changes from 90° to 15° (top to bottom). The block arrows are used to illustrate the direction of compressive loading. The left column (a-f) shows the strains when the scaffold is compressed in the transverse X direction, and the right column (g-l) shows the strains on the same surface but compressed in the transverse Y direction. The red dashed lines are used to calculate average strain values along these lines.

To further compare the strain distribution and transition between different lay-down angles, three different thicknesses were tested for each lay-down angle. In addition to the assembled scaffold in Figure 3, which has three layers in each section of different lay-down angles, two new structures were created, with two and four layers for each section, respectively. The average values of maximum principal strains are calculated along six straight lines on the filament surfaces (red dashed lines in Figure 8) for each layer, respectively (Figure 9). The layers are numbered from 90° to 15°.

It can be seen that all of the three scaffolds show uniform strain distribution within each section, which is independent of the number of layers in the section. When the scaffold is compressed in the transverse X direction, the maximum principal strain increases with decreasing lay-down angles; however, the opposite trend is found when the loading direction is rotated to the transverse Y direction. It can be seen that the strain magnitudes in transverse directions highly depend on the angle between the direction of compressive loading and the filament orientation; the strain is greater when this angle approaches 0° and decreases when this angle approaches 90° (when the loading is perpendicular to the filaments). When the filaments are aligned with the direction of compressive loading, they provide the most preferable path to sustain the mechanical load. On the other hand, when the filaments are perpendicular to the compressive

direction, the load is mainly transferred to neighbor layers, where the filaments are more aligned with the compressive direction.

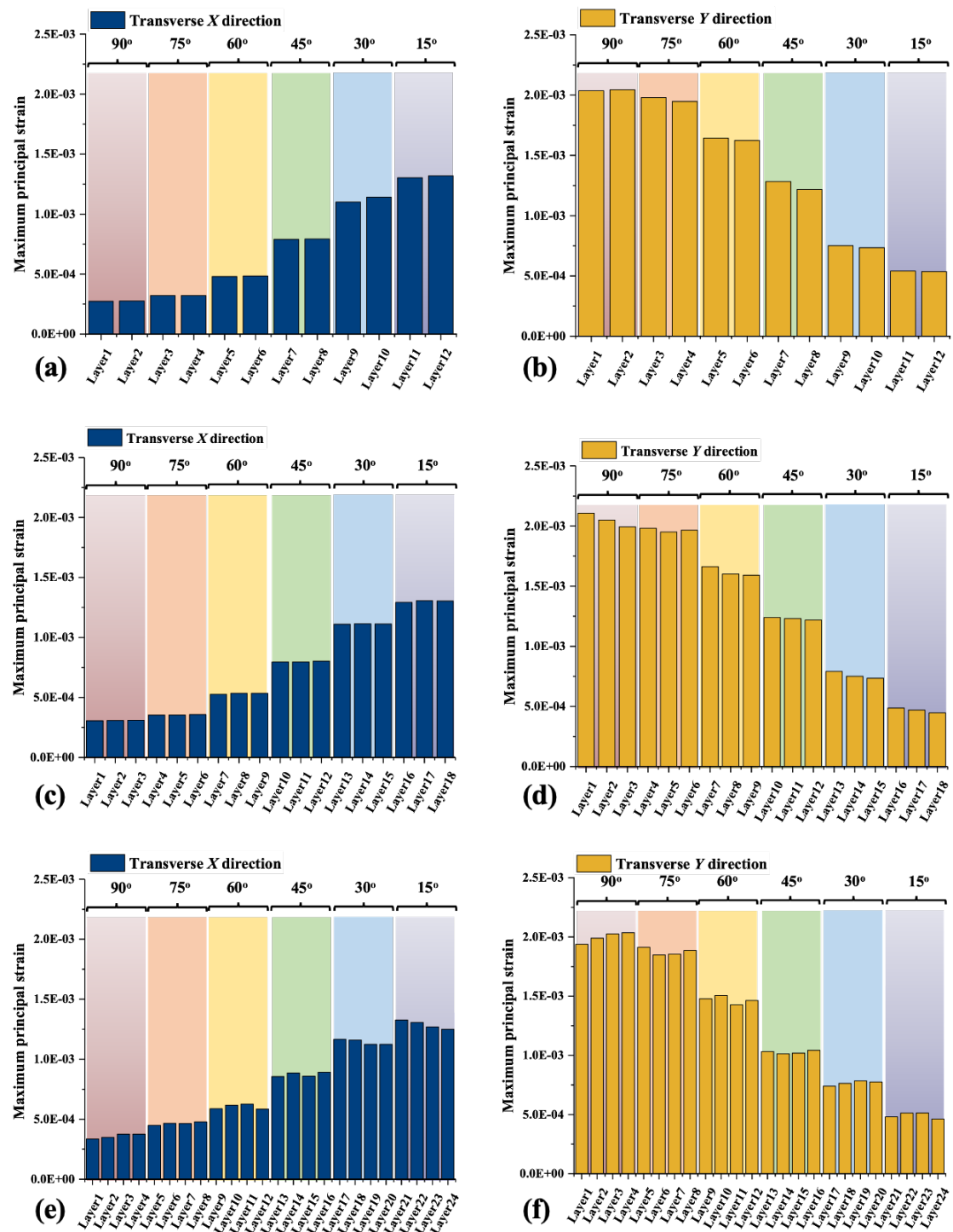Figure 1: Plots of maximum principal strains on filament surfaces compressed in *X* or *Y* direction, which are calculated as average values along the red dashed lines defined in Figure . Three scaffold structures are compared, with two layers (a, b), three layers (c, d), and four layers (e, f) for each section of different lay-down angles, respectively. The layers are numbered from 90° to 15°.

Tunable properties are desirable for bone scaffolds (Feng *et al*., 2018). The combined results of the assembled scaffold and the individual cubic scaffolds with different lay-down angles show that the deformability of the layered lattice scaffolds can be tuned by adjusting the lay-down angles, which represent the pore shapes in porous scaffolds. The various strain magnitudes in different sections of the assembled scaffold are the result of different stiffness values, measured by Young's modulus, in different parts of the scaffold. This approach also indicates that by assembling sections of different lay-down angles together, the final scaffold retains the distinct Young's modulus values exhibited by the individual sections.

It is known that different strain magnitudes can lead to changes in cell differentiation on bone scaffolds (Sumanasinghe *et al*., 2006, Michalopoulos *et al*., 2011, Delaine-Smith and Reilly, 2011). By using an assembled lattice scaffold with multiple lay-down angles, various strain magnitudes and hierarchical/gradient transitions can be achieved in a single construct; a specific strain range at a given location can be accurately adjusted by tuning the local lay-down angle. Using this approach, it is possible to guide cell differentiation in different parts of a given scaffold.

4 Conclusions

This study has investigated the effects of porosity and pore shape on the mechanical properties of 3D lattice scaffolds using finite element modeling. The results show a linear relationship between scaffold porosity and Young's modulus values in the range of osteochondral bone; specifically, the Young's modulus decreases with increasing scaffold porosity. The results also suggest a scaffold porosity value of approximately 60% to separate the scaffold application between cancellous bone repair and cartilage

repair. The cubic scaffolds with a single lay-down angle exhibit the most pronounced isotropic characteristics when the lay-down angle is 90°; the orthotropic effect increases when the lay-down angle decreases from 90° to 15°. Various strain magnitudes and gradient transitions are achieved in a single construct by assembling individual lattice sections with different lay-down angles. These results demonstrate that the hierarchical mechanical characteristics of natural OC tissue can be mimicked by tuning the porosity and local lay-down angles in specific parts of the assembled scaffold. The results also provide guidance on the design of personalized scaffolds using 3D printing technology.

Declaration of competing interest

The authors declare that they have no known competing financial interests or personal relationships that could have appeared to influence the work reported in this paper.

Acknowledgments

Appendix A. Supplementary data

Supplementary data to this article can be found online at
https://doi.org/10.1016/j.jmbbm.2020.103665.

References

ALI, D. & SEN, S. 2017. Finite element analysis of mechanical behavior, permeability and fluid induced wall shear stress of high porosity scaffolds with gyroid and lattice-based architectures. *Journal of the mechanical behavior of biomedical materials,* 75**,** 262-270.

ATHANASIOU, K., AGARWAL, A. & DZIDA, F. 1994. Comparative study of the intrinsic mechanical properties of the human acetabular and femoral head cartilage. *Journal of Orthopaedic Research,* 12**,** 340-349.

BLANCHARD, R., DEJACO, A., BONGAERS, E. & HELLMICH, C. 2013. Intravoxel bone micromechanics for microCT-based finite element simulations. *Journal of biomechanics,* 46**,** 2710-2721.

BOSCHETTI, F., PENNATI, G., GERVASO, F., PERETTI, G. M. & DUBINI, G. 2004. Biomechanical properties of human articular cartilage under compressive loads. *Biorheology,* 41**,** 159-166.

BRYNK, T., HELLMICH, C., FRITSCH, A., ZYSSET, P. & EBERHARDSTEINER, J. 2011. Experimental poromechanics of trabecular bone strength: role of Terzaghi's effective stress and of tissue level stress fluctuations. *Journal of biomechanics,* 44**,** 501-508.

BYRNE, D. P., LACROIX, D., PLANELL, J. A., KELLY, D. J. & PRENDERGAST, P. J. 2007. Simulation of tissue differentiation in a scaffold as a function of porosity, Young's modulus and dissolution rate: application of mechanobiological models in tissue engineering. *Biomaterials,* 28**,** 5544-5554.

CAHILL, S., LOHFELD, S. & MCHUGH, P. E. 2009. Finite element predictions compared to experimental results for the effective modulus of bone tissue engineering scaffolds fabricated by selective laser sintering. *Journal of Materials Science: Materials in Medicine,* 20**,** 1255-1262.

CARTER, D. R., BEAUPRÉ, G. S., GIORI, N. J. & HELMS, J. A. 1998. Mechanobiology of skeletal regeneration. *Clinical orthopaedics and related research,* 355**,** S41-S55.

CHEN, D., WEI, J., DENG, Y., XU, H., LI, Z., MENG, H., HAN, X., WANG, Y., WAN, J. & YAN, T. 2018. Virtual stenting with simplex mesh and mechanical contact analysis for real-time planning of thoracic endovascular aortic repair. *Theranostics,* 8**,** 5758.

CHEN, Y., FENG, B., ZHU, Y., WENG, J., WANG, J. & LU, X. 2011. Preparation and characterization of a novel porous titanium scaffold with 3D hierarchical porous structures. *Journal of Materials Science: Materials in Medicine,* 22**,** 839-844.

CHIANG, H. & JIANG, C.-C. 2009. Repair of articular cartilage defects: review and perspectives. *Journal of the Formosan Medical Association,* 108**,** 87-101.

DEJACO, A., KOMLEV, V. S., JAROSZEWICZ, J., SWIESZKOWSKI, W. & HELLMICH, C. 2012. Micro CT-based multiscale elasticity of double-porous (pre-cracked) hydroxyapatite granules for regenerative medicine. *Journal of Biomechanics,* 45**,** 1068-1075.

DELAINE-SMITH, R. M. & REILLY, G. C. 2011. The effects of mechanical loading on mesenchymal stem cell differentiation and matrix production. *Vitamins & Hormones.* Elsevier.

DIEGO, R. B., ESTELLÉS, J. M., SANZ, J. A., GARCÍA‐AZNAR, J. M. & SÁNCHEZ, M. S. 2007. Polymer scaffolds with interconnected spherical pores and controlled architecture for tissue engineering: fabrication, mechanical properties, and finite element modeling. *Journal of Biomedical Materials Research Part B: Applied Biomaterials: An Official Journal of The Society for Biomaterials, The Japanese Society for Biomaterials, and The Australian Society for Biomaterials and the Korean Society for Biomaterials,* 81**,** 448-455.

DO, A. V., KHORSAND, B., GEARY, S. M. & SALEM, A. K. 2015. 3D printing of scaffolds for tissue regeneration applications. *Advanced healthcare materials,* 4**,** 1742-1762.

DOMINGOS, M., INTRANUOVO, F., RUSSO, T., DE SANTIS, R., GLORIA, A., AMBROSIO, L., CIURANA, J. & BARTOLO, P. 2013. The first systematic analysis of 3D rapid prototyped poly (ε-caprolactone) scaffolds manufactured through BioCell printing: the effect of pore size and geometry on compressive mechanical behaviour and in vitro hMSC viability. *Biofabrication,* 5**,** 045004.

DORCEMUS, D. L. & NUKAVARAPU, S. P. 2014. Novel and unique matrix design for osteochondral tissue engineering. *MRS Online Proceedings Library Archive,* 1621**,** 17-23.

DORMER, N. H., SINGH, M., WANG, L., BERKLAND, C. J. & DETAMORE, M. S. 2010. Osteochondral interface tissue engineering using macroscopic gradients of bioactive signals. *Annals of biomedical engineering,* 38**,** 2167-2182.

ENTEZARI, A., ZHANG, Z., SUE, A., SUN, G., HUO, X., CHANG, C.-C., ZHOU, S., SWAIN, M. V. & LI, Q. 2019. Nondestructive characterization of bone tissue scaffolds for clinical scenarios. *Journal of the mechanical behavior of biomedical materials,* 89**,** 150-161.

ESHRAGHI, S. & DAS, S. 2010. Mechanical and microstructural properties of polycaprolactone scaffolds with one-dimensional, two-dimensional, and three-dimensional orthogonally oriented porous architectures produced by selective laser sintering. *Acta biomaterialia,* 6**,** 2467-2476.

FENG, P., KONG, Y., YU, L., LI, Y., GAO, C., PENG, S., PAN, H., ZHAO, Z. & SHUAI, C. 2019. Molybdenum disulfide nanosheets embedded with nanodiamond particles: co-dispersion nanostructures as reinforcements for polymer scaffolds. *Applied Materials Today,* 17**,** 216-226.

FENG, P., NIU, M., GAO, C., PENG, S. & SHUAI, C. 2014. A novel two-step sintering for nano-hydroxyapatite scaffolds for bone tissue engineering. *Scientific reports,* 4**,** 5599.

FENG, P., WU, P., GAO, C., YANG, Y., GUO, W., YANG, W. & SHUAI, C. 2018. A multimaterial scaffold with tunable properties: toward bone tissue repair. *Advanced Science,* 5.

FRITSCH, A., DORMIEUX, L., HELLMICH, C. & SANAHUJA, J. 2009. Mechanical behavior of hydroxyapatite biomaterials: an experimentally validated micromechanical model for elasticity and strength. *Journal of Biomedical Materials Research Part A: An Official Journal of The Society for Biomaterials, The Japanese Society for Biomaterials, and The Australian Society for Biomaterials and the Korean Society for Biomaterials,* 88**,** 149-161.

FRITSCH, A., HELLMICH, C. & DORMIEUX, L. 2010. The role of disc-type crystal shape for micromechanical predictions of elasticity and strength of hydroxyapatite biomaterials. *Philosophical Transactions of the Royal Society A: Mathematical, Physical and Engineering Sciences,* 368**,** 1913-1935.

GIBSON, L. J. 1985. The mechanical behaviour of cancellous bone. *Journal of biomechanics,* 18**,** 317-328.

GÓMEZ, S., VLAD, M., LÓPEZ, J. & FERNÁNDEZ, E. 2016. Design and properties of 3D scaffolds for bone tissue engineering. *Acta biomaterialia,* 42**,** 341-350.

GÓMEZ, S., VLAD, M. D., LÓPEZ, J., NAVARRO, M. & FERNÁNDEZ, E. 2013. Characterization and three-dimensional reconstruction of synthetic bone model foams. *Materials Science and Engineering: C,* 33**,** 3329-3335.

GONÇALVES, E. M., OLIVEIRA, F. J., SILVA, R. F., NETO, M. A., FERNANDES, M. H., AMARAL, M., VALLET‐REGÍ, M. & VILA, M. 2016. Three‐dimensional printed PCL‐hydroxyapatite scaffolds filled with CNTs for bone cell growth stimulation. *Journal of Biomedical Materials Research Part B: Applied Biomaterials,* 104**,** 1210-1219.

GUO, L., VARDAKIS, J. C., CHOU, D. & VENTIKOS, Y. 2020. A multiple-network poroelastic model for biological systems and application to subject-specific modelling of cerebral fluid transport. *International Journal of Engineering Science,* 147**,** 103204.

GUO, L., VARDAKIS, J. C., LASSILA, T., MITOLO, M., RAVIKUMAR, N., CHOU, D., LANGE, M., SARRAMI-FOROUSHANI, A., TULLY, B. J. & TAYLOR, Z. A. 2017. Subject-specific multi-poroelastic model for exploring the risk factors associated with the early stages of Alzheimer's disease. *Interface focus,* 8**,** 20170019.

HELLMICH, C., ULM, F.-J. & DORMIEUX, L. 2004. Can the diverse elastic properties of trabecular and cortical bone be attributed to only a few tissue-independent phase properties and their interactions? *Biomechanics and modeling in mechanobiology,* 2**,** 219-238.

HENDRIKSON, W. J., DEEGAN, A. J., YANG, Y., VAN BLITTERSWIJK, C. A., VERDONSCHOT, N., MORONI, L. & ROUWKEMA, J. 2017. Influence of additive manufactured scaffold architecture on the distribution of surface strains and fluid flow shear stresses and expected osteochondral cell differentiation. *Frontiers in bioengineering and biotechnology,* 5**,** 6.

HUANG, J., BEST, S., BONFIELD, W. & BUCKLAND, T. 2010. Development and characterization of titanium-containing hydroxyapatite for medical applications. *Acta biomaterialia,* 6**,** 241-249.

HULBERT, S., YOUNG, F., MATHEWS, R., KLAWITTER, J., TALBERT, C. & STELLING, F. 1970. Potential of ceramic materials as permanently implantable skeletal prostheses. *Journal of biomedical materials research,* 4**,** 433-456.

HUTMACHER, D. & COOL, S. 2007. Concepts of scaffold‐based tissue engineering−the rationale to use solid free‐form fabrication techniques. *Journal of cellular and molecular medicine,* 11**,** 654-669.

JAKOB, R. P., FRANZ, T., GAUTIER, E. & MAINIL-VARLET, P. 2002. Autologous osteochondral grafting in the knee: indication, results, and reflections. *Clinical orthopaedics and related research,* 401**,** 170-184.

JIANG, J., TANG, A., ATESHIAN, G. A., GUO, X. E., HUNG, C. T. & LU, H. H. 2010. Bioactive stratified polymer ceramic-hydrogel scaffold for integrative osteochondral repair. *Annals of biomedical engineering,* 38**,** 2183-2196.

KAPLAN, S. J., HAYES, W. C., STONE, J. L. & BEAUPRÉ, G. S. 1985. Tensile strength of bovine trabecular bone. *Journal of biomechanics,* 18**,** 727.

KARIEM, H., PASTRAMA, M.-I., ROOHANI-ESFAHANI, S. I., PIVONKA, P., ZREIQAT, H. & HELLMICH, C. 2015. Micro-poro-elasticity of baghdadite-based bone tissue engineering scaffolds: a unifying approach based on

ultrasonics, nanoindentation, and homogenization theory. *Materials Science and Engineering: C,* 46**,** 553-564.

KAUL, H., HALL, B. K., NEWBY, C. & VENTIKOS, Y. 2015. Synergistic activity of polarised osteoblasts inside condensations cause their differentiation. *Scientific reports,* 5**,** 11838.

KÖNIGSBERGER, M., PICHLER, B. & HELLMICH, C. 2020. Multiscale poro-elasticity of densifying calcium-silicate hydrates in cement paste: An experimentally validated continuum micromechanics approach. *International Journal of Engineering Science,* 147**,** 103196.

LACROIX, D., CHATEAU, A., GINEBRA, M.-P. & PLANELL, J. A. 2006. Micro-finite element models of bone tissue-engineering scaffolds. *Biomaterials,* 27**,** 5326-5334.

LACROIX, D. & PRENDERGAST, P. 2002. A mechano-regulation model for tissue differentiation during fracture healing: analysis of gap size and loading. *Journal of biomechanics,* 35**,** 1163-1171.

LOH, Q. L. & CHOONG, C. 2013. Three-dimensional scaffolds for tissue engineering applications: role of porosity and pore size. *Tissue Engineering Part B: Reviews,* 19**,** 485-502.

LUCZYNSKI, K., DEJACO, A., LAHAYNE, O., JAROSZEWICZ, J., SWIESZKOWSKI, W. & HELLMICH, C. 2012. MicroCT/micromechanics-based finite element models and quasi-static unloading tests deliver consistent values for Young's modulus of rapid-prototyped polymer-ceramic tissue engineering scaffold. *Computer Modeling in Engineering & Sciences(CMES),* 87**,** 505-528.

LUCZYNSKI, K. W., BRYNK, T., OSTROWSKA, B., SWIESZKOWSKI, W., REIHSNER, R. & HELLMICH, C. 2013. Consistent quasistatic and acoustic elasticity determination of poly‐l‐lactide‐based rapid‐prototyped tissue engineering scaffolds. *Journal of Biomedical Materials Research Part A,* 101**,** 138-144.

MELCHELS, F. P., BERTOLDI, K., GABBRIELLI, R., VELDERS, A. H., FEIJEN, J. & GRIJPMA, D. W. 2010. Mathematically defined tissue engineering scaffold architectures prepared by stereolithography. *Biomaterials,* 31**,** 6909-6916.

MEYER, U., BÜCHTER, A., NAZER, N. & WIESMANN, H. 2006. Design and performance of a bioreactor system for mechanically promoted three-dimensional tissue engineering. *British Journal of Oral and Maxillofacial Surgery,* 44**,** 134-140.

MICHALOPOULOS, E., KNIGHT, R. L., KOROSSIS, S., KEARNEY, J. N., FISHER, J. & INGHAM, E. 2011. Development of methods for studying the differentiation of human mesenchymal stem cells under cyclic compressive strain. *Tissue Engineering Part C: Methods,* 18**,** 252-262.

MOBASHERI, A., KALAMEGAM, G., MUSUMECI, G. & BATT, M. E. 2014. Chondrocyte and mesenchymal stem cell-based therapies for cartilage repair in osteoarthritis and related orthopaedic conditions. *Maturitas,* 78**,** 188-198.

NAGHIEH, S., KARAMOOZ-RAVARI, M. R., SARKER, M., KARKI, E. & CHEN, X. 2018. Influence of crosslinking on the mechanical behavior of 3D printed alginate scaffolds: Experimental and numerical approaches. *Journal of the mechanical behavior of biomedical materials,* 80**,** 111-118.

NAGHIEH, S., RAVARI, M. K., BADROSSAMAY, M., FOROOZMEHR, E. & KADKHODAEI, M. 2016. Numerical investigation of the mechanical

properties of the additive manufactured bone scaffolds fabricated by FDM: The effect of layer penetration and post-heating. *Journal of the mechanical behavior of biomedical materials,* 59**,** 241-250.

NOOEAID, P., SALIH, V., BEIER, J. P. & BOCCACCINI, A. R. 2012. Osteochondral tissue engineering: scaffolds, stem cells and applications. *Journal of cellular and molecular medicine,* 16**,** 2247-2270.

PARK, S. A., LEE, S. H. & KIM, W. D. 2011. Fabrication of porous polycaprolactone/hydroxyapatite (PCL/HA) blend scaffolds using a 3D plotting system for bone tissue engineering. *Bioprocess and biosystems engineering,* 34**,** 505-513.

PRENDERGAST, P., HUISKES, R. & SØBALLE, K. 1997. Biophysical stimuli on cells during tissue differentiation at implant interfaces. *Journal of biomechanics,* 30**,** 539-548.

RAGHUNATH, J., ROLLO, J., SALES, K. M., BUTLER, P. E. & SEIFALIAN, A. M. 2007. Biomaterials and scaffold design: key to tissue‐engineering cartilage. *Biotechnology and applied biochemistry,* 46**,** 73-84.

REICHERT, J. C., WULLSCHLEGER, M. E., CIPITRIA, A., LIENAU, J., CHENG, T. K., SCHÜTZ, M. A., DUDA, G. N., NÖTH, U., EULERT, J. & HUTMACHER, D. W. 2011. Custom-made composite scaffolds for segmental defect repair in long bones. *International orthopaedics,* 35**,** 1229-1236.

RENDERS, G., MULDER, L., LANGENBACH, G., VAN RUIJVEN, L. & VAN EIJDEN, T. 2008. Biomechanical effect of mineral heterogeneity in trabecular bone. *Journal of Biomechanics,* 41**,** 2793-2798.

REZWAN, K., CHEN, Q., BLAKER, J. & BOCCACCINI, A. R. 2006. Biodegradable and bioactive porous polymer/inorganic composite scaffolds for bone tissue engineering. *Biomaterials,* 27**,** 3413-3431.

RODRIGUES, M. T., GOMES, M. E. & REIS, R. L. 2011. Current strategies for osteochondral regeneration: from stem cells to pre-clinical approaches. *Current opinion in biotechnology,* 22**,** 726-733.

RODRÍGUEZ-MONTAÑO, Ó. L., CORTÉS-RODRÍGUEZ, C. J., UVA, A. E., FIORENTINO, M., GATTULLO, M., MONNO, G. & BOCCACCIO, A. 2018. Comparison of the mechanobiological performance of bone tissue scaffolds based on different unit cell geometries. *Journal of the mechanical behavior of biomedical materials,* 83**,** 28-45.

SABREE, I., GOUGH, J. & DERBY, B. 2015. Mechanical properties of porous ceramic scaffolds: influence of internal dimensions. *Ceramics International,* 41**,** 8425-8432.

SAN CHEONG, V., FROMME, P., MUMITH, A., COATHUP, M. J. & BLUNN, G. W. 2018. Novel adaptive finite element algorithms to predict bone ingrowth in additive manufactured porous implants. *Journal of the mechanical behavior of biomedical materials,* 87**,** 230-239.

SANDINO, C., PLANELL, J. & LACROIX, D. 2008. A finite element study of mechanical stimuli in scaffolds for bone tissue engineering. *Journal of biomechanics,* 41**,** 1005-1014.

SCHAEFER, D., MARTIN, I., SHASTRI, P., PADERA, R., LANGER, R., FREED, L. & VUNJAK-NOVAKOVIC, G. 2000. In vitro generation of osteochondral composites. *Biomaterials,* 21**,** 2599-2606.

SCHEINER, S., SINIBALDI, R., PICHLER, B., KOMLEV, V., RENGHINI, C., VITALE-BROVARONE, C., RUSTICHELLI, F. & HELLMICH, C. 2009.

Micromechanics of bone tissue-engineering scaffolds, based on resolution error-cleared computer tomography. *Biomaterials,* 30**,** 2411-2419.

SCHEK, R. M., TABOAS, J. M., SEGVICH, S. J., HOLLISTER, S. J. & KREBSBACH, P. H. 2004. Engineered osteochondral grafts using biphasic composite solid free-form fabricated scaffolds. *Tissue Engineering,* 10**,** 1376-1385.

SCHROEDER, J. E. & MOSHEIFF, R. 2011. Tissue engineering approaches for bone repair: concepts and evidence. *Injury,* 42**,** 609-613.

SHUAI, C., FENG, P., WU, P., LIU, Y., LIU, X., LAI, D., GAO, C. & PENG, S. 2017. A combined nanostructure constructed by graphene and boron nitride nanotubes reinforces ceramic scaffolds. *Chemical Engineering Journal,* 313**,** 487-497.

SHUAI, C., GUO, W., WU, P., YANG, W., HU, S., XIA, Y. & FENG, P. 2018. A graphene oxide-Ag co-dispersing nanosystem: dual synergistic effects on antibacterial activities and mechanical properties of polymer scaffolds. *Chemical Engineering Journal,* 347**,** 322-333.

SHUAI, C., LIU, G., YANG, Y., YANG, W., HE, C., WANG, G., LIU, Z., QI, F. & PENG, S. 2020a. Functionalized BaTiO3 enhances piezoelectric effect towards cell response of bone scaffold. *Colloids and Surfaces B: Biointerfaces,* 185**,** 110587.

SHUAI, C., YANG, W., HE, C., PENG, S., GAO, C., YANG, Y., QI, F. & FENG, P. 2020b. A magnetic micro-environment in scaffolds for stimulating bone regeneration. *Materials & Design,* 185**,** 108275.

SHUAI, C., ZAN, J., YANG, Y., PENG, S., YANG, W., QI, F., SHEN, L. & TIAN, Z. 2020c. Surface modification enhances interfacial bonding in PLLA/MgO bone scaffold. *Materials Science and Engineering: C,* 108**,** 110486.

SOPHIA FOX, A. J., BEDI, A. & RODEO, S. A. 2009. The basic science of articular cartilage: structure, composition, and function. *Sports health,* 1**,** 461-468.

SUMANASINGHE, R. D., BERNACKI, S. H. & LOBOA, E. G. 2006. Osteogenic differentiation of human mesenchymal stem cells in collagen matrices: effect of uniaxial cyclic tensile strain on bone morphogenetic protein (BMP-2) mRNA expression. *Tissue engineering,* 12**,** 3459-3465.

SUTCU, M. 1992. Orthotropic and transversely isotropic stress-strain relations with built-in coordinate transformations. *International journal of solids and structures,* 29**,** 503-518.

SZLAZAK, K., VASS, V., HASSLINGER, P., JAROSZEWICZ, J., DEJACO, A., IDASZEK, J., SCHEINER, S., HELLMICH, C. & SWIESZKOWSKI, W. 2019. X-ray physics-based CT-to-composition conversion applied to a tissue engineering scaffold, enabling multiscale simulation of its elastic behavior. *Materials Science and Engineering: C,* 95**,** 389-396.

TRACHTENBERG, J. E., PLACONE, J. K., SMITH, B. T., FISHER, J. P. & MIKOS, A. G. 2017. Extrusion-based 3D printing of poly (propylene fumarate) scaffolds with hydroxyapatite gradients. *Journal of Biomaterials Science, Polymer Edition,* 28**,** 532-554.

VACANTI, J. P. & LANGER, R. 1999. Tissue engineering: the design and fabrication of living replacement devices for surgical reconstruction and transplantation. *The lancet,* 354**,** S32-S34.

VAN BAEL, S., Chai, Y. C., TRUSCELLO, S., MOESEN, M., KERCKHOFS, G., VAN OOSTERWYCK, H., KRUTH, J. P. & SCHROOTEN, J. 2012. The effect of pore geometry on the in vitro biological behavior of human periosteum-

derived cells seeded on selective laser-melted Ti6Al4V bone scaffolds. *Acta Biomaterialia,* 8**,** 2824–2834.

VAN RIETBERGEN, B., MÜLLER, R., ULRICH, D., RÜEGSEGGER, P. & HUISKES, R. 1999. Tissue stresses and strain in trabeculae of a canine proximal femur can be quantified from computer reconstructions. *Journal of biomechanics,* 32**,** 165-173.

WANG, H., SU, K., SU, L., LIANG, P., JI, P. & WANG, C. 2018. The effect of 3D-printed Ti6Al4V scaffolds with various macropore structures on osteointegration and osteogenesis: A biomechanical evaluation. *Journal of the mechanical behavior of biomedical materials,* 88**,** 488-496.

WILLIAMS, J. & LEWIS, J. 1982. Properties and an anisotropic model of cancellous bone from the proximal tibial epiphysis. *Journal of biomechanical engineering,* 104**,** 50-56.

WÜST, S., MÜLLER, R. & HOFMANN, S. 2011. Controlled positioning of cells in biomaterials—approaches towards 3D tissue printing. *Journal of functional biomaterials,* 2**,** 119-154.

YANG, Y., YUAN, F., GAO, C., FENG, P., XUE, L., HE, S. & SHUAI, C. 2018. A combined strategy to enhance the properties of Zn by laser rapid solidification and laser alloying. *Journal of the mechanical behavior of biomedical materials,* 82**,** 51-60.